ACS APPLIED MATERIALS & INTERFACES

Research Article

Cite This: ACS Appl. Mater. Interfaces 2019, 11, 3753−3762

www.acsami.org

Biosensor for Point-of-Care Analysis of Immunoglobulins in Urine by Metal Enhanced Fluorescence from Gold Nanoparticles

Bartolomeo Della Ventura,[†] Monica Gelzo,[‡,§] Edmondo Battista,[*,∥] Alessandro Alabastri,[⊥] Andrea Schirato,[#] Giuseppe Castaldo,[‡,§] Gaetano Corso,[▽] Francesco Gentile,[*,○] and Raffaele Velotta[*,†]

[†]Dipartimento di Fisica *Ettore Pancini*, Università di Napoli Federico II, Via Cintia, 26 Ed. 6, 80126 Napoli, Italy

[‡]Dipartimento di Medicina Molecolare e Biotecnologie Mediche, Università di Napoli Federico II, Via Pansini 5, 80131 Napoli, Italy

[§]CEINGE-Biotecnologie avanzate s.c. a r.l., Via Gaetano Salvatore 486, 80145 Napoli, Italy

[∥]Centro di Ricerca Interdipartimentale sui Biomateriali, Università degli Studi di Napoli "Federico II", Ple Tecchio 80, 80125 Napoli, Italy

[⊥]Electrical and Computer Engineering Department, Rice University, 6100 Main Street, Houston, Texas 77005, United States

[#]Dipartimento di Fisica, Politecnico di Milano, Piazza L. da Vinci 32, 20133 Milano, Italy

[▽]Dipartimento di Medicina Clinica e Sperimentale, Università di Foggia, 70122 Viale Pinto, Foggia, Italy

[○]Dipartimento di Ingegneria Elettrica e Tecnologie dell'Informazione, Università di Napoli Federico II, via Claudio 21, 80125 Napoli, Italy

Supporting Information

ABSTRACT: Biosensors are easy-to-use and cost-effective devices that are emerging as an attractive tool, not only in settling diagnosis or in disease monitoring, but also in mass screening tests, a timely topic that impacts on daily life of the whole society. Nanotechnologies lend themselves to the development of highly sensitive devices whose realization has become a very interdisciplinary topic. Relying on the enhancement of the fluorescence signal detected at the surface of patterned gold nanoparticles, we report the behavior of an analytical device in detecting immunoglobulins in real urine samples that shows a limit of detection of approximately 8 μg/L and a linear range of 10−100 μg/L well below the detection limit of nephelometric method, which is the reference method for this analysis. These performances have been reached thanks to an effective surface functionalization technique and can be improved even more if superydrophobic features of the substrate we produce will be exploited. Since the analyte recognition is realized by antibodies the specificity is very high and, in fact, no interference has been detected by other compounds also present in the real urine samples. The device has been assessed on serum samples by comparing IgG concentrations values obtained by the biosensor with those provided by a nephelometer. In this step we found that our approach allows the analysis of the whole blood without any pretreatment; moreover, it is inherently extendable to the analysis of most biochemical markers in biological fluids.

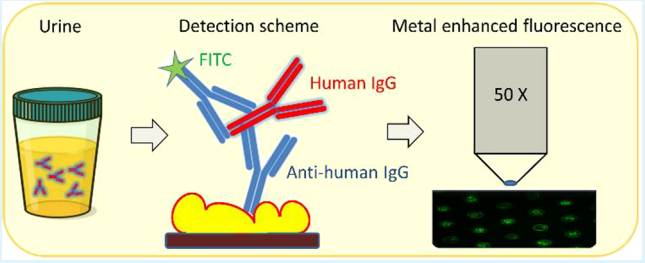

KEYWORDS: *point-of-care device, biosensors, metal enhanced fluorescence, photochemical immobilization technique, antibody, nanostructured gold surface, gold nanoparticles*

INTRODUCTION

The quest for reliable point-of-care (POC) devices is underpinning a growing research area where the interdisciplinary approach is crucial in view of the challenges represented by the realization of a device in which easiness-to-use and fast response has to be combined with high analytical sensitivity and specificity.[1] Biosensors can be the key to successful POC devices in all the situations where a precise detection of biomolecules is necessary for settling diagnosis and/or monitoring acute and chronic illnesses.[2] In this respect, the advent of nanotechnology is making it even truer[3] also in view of applications of nanotech-based biosensors to the so-called precision medicine, a sophisticated evolution of the conventional medicine, where treatment of a disease, patient care, medical interventions, and the administration of therapeutics, are tailored to individual patients and are based on an accurate assessment of the conditions of a patient.[4] In fact, precise determination of the state of a patient implicates detection and

Received: November 21, 2018
Accepted: January 4, 2019
Published: January 4, 2019

DOI: 10.1021/acsami.8b20501
ACS Appl. Mater. Interfaces 2019, 11, 3753−3762

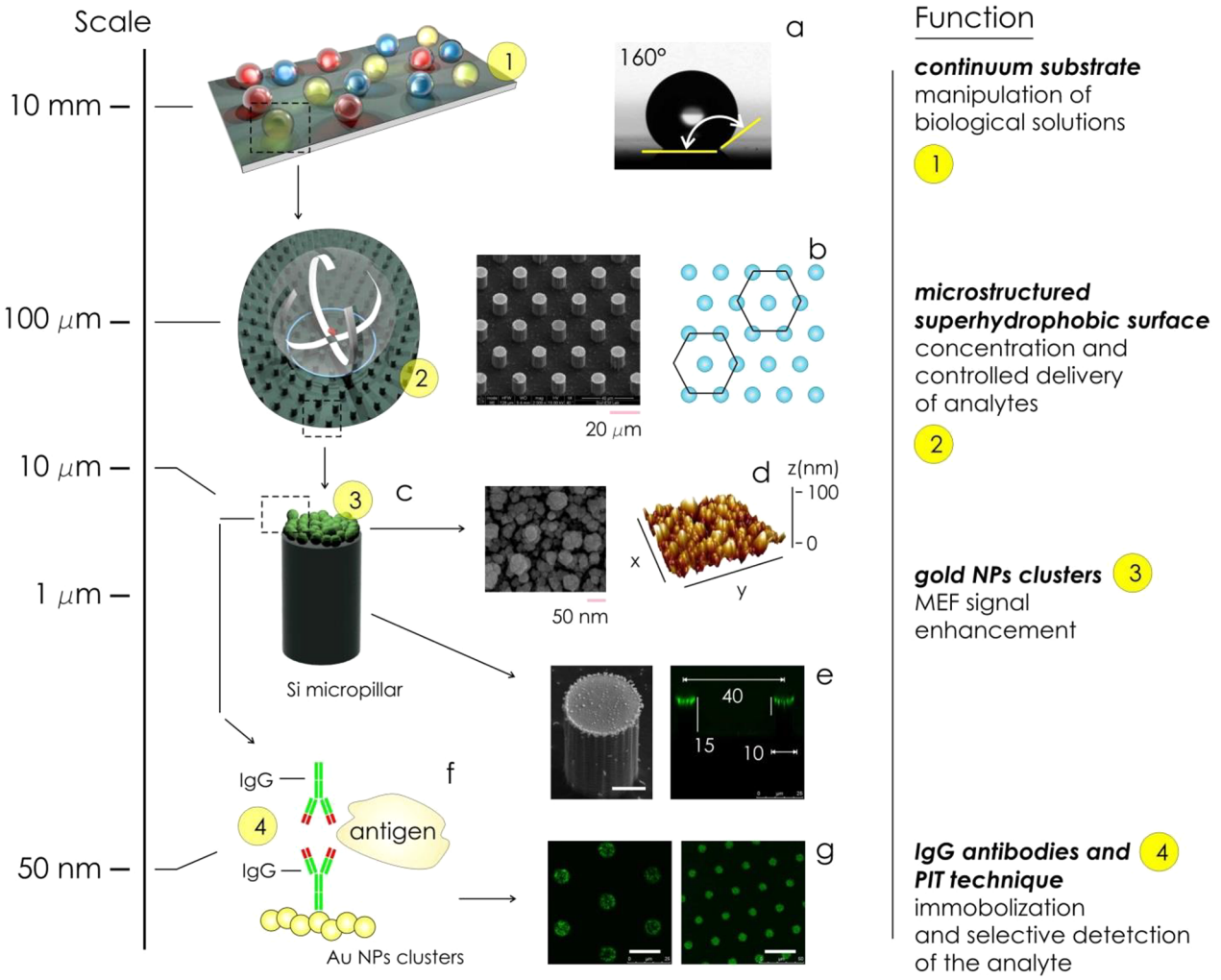

Figure 1. Artistic representation of the device. The device exhibits different functions at different scales. (a) At the continuum macroscale, the substrate presents superhydrophobic characteristics, whereby biological solutions can be easily manipulated. (b) At the microscale, array of superhydrophobic pillars enforces the solution to maintain a spherical shape and regulate site-selective delivery of the analytes in solution to the gold nanoparticles on the pillar surface. (c) At the nanoscale, clusters of gold nanoparticles (d) enable metal enhanced fluorescence effects (e). (f) Biological functionalization of gold particles allows selective capture of immunoglobulins that can be readily detected by the device (g) in vanishingly low abundance ranges.

diagnosis of diseases with high spatial and temporal resolution, high sensitivity and elevated specificity, properties that are not generally achieved by all analytical techniques, medicine functional imaging techniques, or other traditional molecular techniques of analysis. Since micro- and nano-scale systems enable a direct interaction with the biological molecular markers of a disease, they are the ideal candidates for pathology screening; for these systems, details at arbitrarily small scales translate to improved information quality, quantity, and density;[5] thus, much of precision medicine coincides with nanotechnology.[6−10]

In electrochemical and organic electrochemical transistor (OECT) biosensors, nanoscale modification of the surface improves the sensitivity of the measurements, enables selectivity, and enhances resolution. Micro- and nanoscale patterns, and their combination, enable biomolecule localization at precise sites of the device, amplify signal, amplify signal differences between species, and accelerate the process of electron transfer at the interface with the biological liquids.[11,12] Nevertheless, while electrochemical transduction of the ionic strength of a solution into an electric signal permits simple signal acquisition, manipulation, and analysis, and frees from the need of a calibration standard, multiple components in a solution may blur the output of the device and make the problem of decoding the information content of a mixture inherently untreatable. Electrochemical devices show a low efficiency in resolving complex mixtures when the components of the mixtures are more than two, unless one uses convenient pre and post processing of data, mathematical models and algorithms that help in interpreting data and finding hidden patterns in them.[11,13]

In contrast to electrochemical sensing, optical methods allow recognition of molecules even in the presence of noise, that is, in complex mixtures, with high sensitivity and reproducibility. The resulting devices are typically rugged to be easily handled; moreover, the control of the surface geometry and topography is a formidable tool for manipulating the electromagnetic radiation at localized area, this resulting in an enhancement of the signal strength and of the device response by several orders of magnitude.[14−17] In particular, metal-enhanced-fluorescence (MEF) provides an increased emission of characteristic electromagnetic radiation from an analyte that is in proximity

DOI: 10.1021/acsami.8b20501
ACS Appl. Mater. Interfaces 2019, 11, 3753−3762

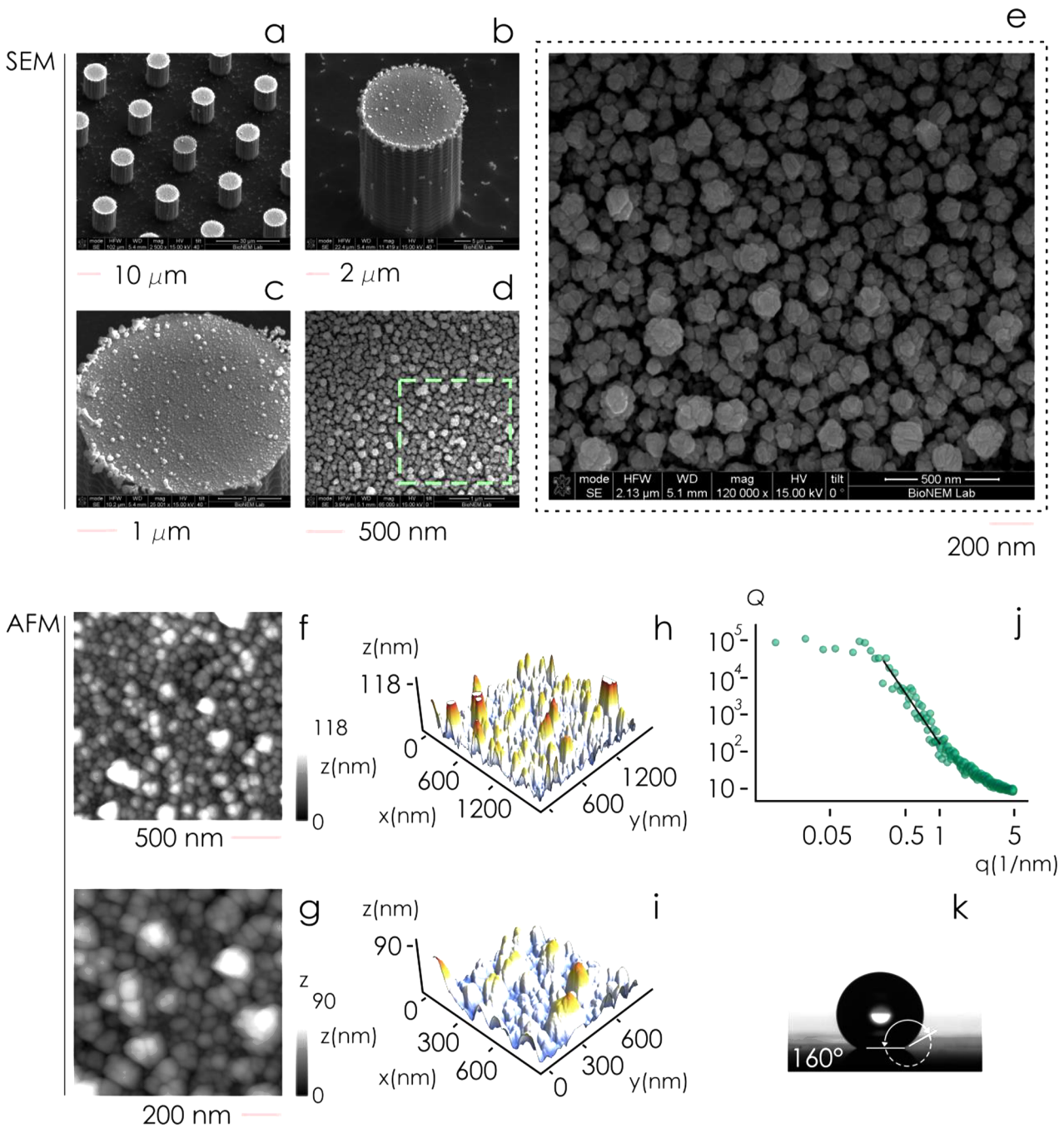

Figure 2. (a) SEM micrographs of sample surface at low magnification demonstrate the repetition of superhydrophobic micropillars over large areas. (b)−(d) Individual pillars are covered by clusters of gold-nanoparticles. (e) High-magnification SEM images of the upper surface of the pillars reveal the topography of the gold nanoparticles at the nanoscale. The topography of the clusters of golf nanoparticles was further examined using (f, h) high and (g, (i) ultrahigh resolution AFM imaging of samples. (j) AFM data were used to derive the power spectrum density function of the clusters of gold nanoparticles, which was used to derive, in turn, the fractal dimensions of sample surface. (k) Due to a multiscale design, substrates are superhydrophobic with measured contact angles as high as 160°.

to a plasmonic nanostructured surface,[15,18] thus unprecedented limit of detection (LOD) can be reached even with ordinary fluorescence microscopes.

Here, we present a functionalized, superhydrophobic optical device that achieves prompt detection of human IgG immunoglobulins in urine samples with high analytical sensitivity and accuracy. The device comprises arrays of cylindrical micropillars decorated with clusters of gold nanoparticles functionalized with antibodies (Abs) for selective capture of human IgG. The device takes advantage from the integration of different hierarchical scales. At the millimeter scale, the device shows a macroscopic, continuum level response and enables sample manipulation, handling and control (Figure 1a). At the micro scale, superhydrophobic pillars enable concentration and precise delivery of analytes from the sample to the active sites of the device[19] (Figure 1b). At the nanometer scale, MEF[20−25] induced by clusters of gold nanoparticles allows one to measure the fluorescence with very high sensitivity, even in no high-end fluorescence systems (Figure 1c). In the scheme, Abs are anchored to the gold

DOI: 10.1021/acsami.8b20501
ACS Appl. Mater. Interfaces 2019, 11, 3753−3762

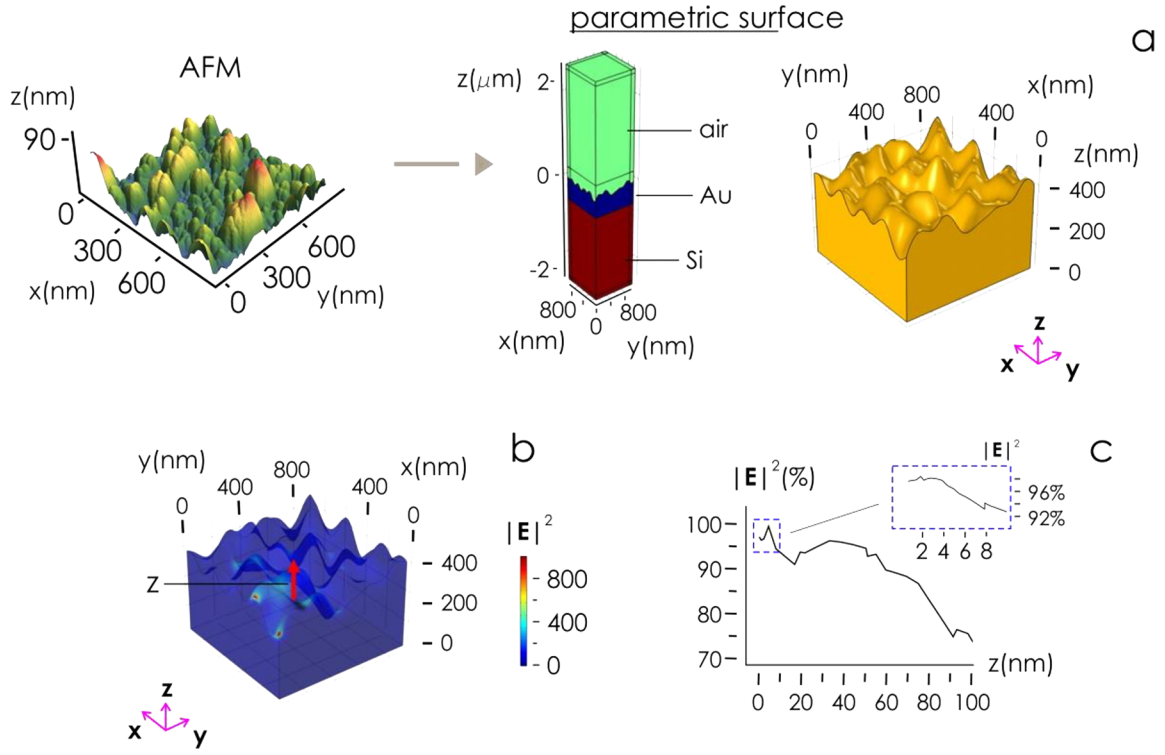

Figure 3. Numerical schemes were used to simulate the EM field around the clusters of gold-nanoparticles. (a) The geometrical model in the simulations was reconstructed from the AFM profile of the real surfaces. (b) Direct FEM simulations indicate that the intensity of the EM field on the gold nanoparticles surface is up to 1000 times the intensity of the incident EM radiation and (c) decreases to the 60% of this value 60 nm perpendicularly away from the interface.

nanoparticles through an original photochemical immobilization technique (PIT) developed by some of the authors of the paper[26] (Figure 1d).

The combination of a nanostructured material with an efficient functionalization technique allowed us to realize an immunosensor, which has proven to be effective in the detection of IgG in complex matrices like urine with a limit of detection lower than 10 μg/L. The device has been assessed by comparing the measurement of the concentration of IgG in serum (after dilutions 1:10 000−100 000) carried out by the biosensor to the results provided by a nephelometer on the undiluted serum. The agreement between the results provided by the two methods is more than satisfactory allowing us to apply the biosensors on real biological samples.

The easiness to use and the cost effectiveness of the analytical procedure proposed in the present work make the biosensor suitable for bedside and point-of-care applications as well as for mass screening tests. This perspective is even more realistic when it is considered that IgG concentration could be measured directly in blood with no pretreatment but dilution.

RESULTS AND DISCUSSION

Generating Superhydrophobic Plasmonic Devices. Several SEM images were taken to assess the fabrication process capability to generate arrays of superhydrophobic micropillars over large areas, with tight control over the size and shape of the pillars (Figure 2a). Each silicon pillar is a cylinder with diameter d = 10 μm and height h = 15 μm, spacing between pillars is δ = 20 μm (Figures 2a,b). Ratio between diameter and spacing is such that the packing factor $\phi = \pi/4(d/\delta)^2 \sim 0.087$ (ϕ is the fraction of volume in the plane that is occupied by pillars), that with Cassie and Baxter[27] guarantees superhydrophobicity of the device with contact angles $\theta_f > 150°$ for any initial angle of contact θ_i on the nontextured surface $\theta_i \geq 60°$ (the contact angles of a water droplet on a superhydrophobic material exceed 150°). Ratio between height and diameter h/d = 1.5 enables stable adhesion of a drop on the surface and prevents early collapse of the drop shortly after deposition.[28] The upper surface of the pillars is decorated with clusters of gold nanoparticles assembled by electroless deposition techniques (Figure 2c,d). Larger particles in the clusters have a size $s \sim 100$ nm, smaller particles have a size $s \sim 30$ nm. Average particle size is $\langle s \rangle \sim 60$ nm with standard deviation $\sigma \sim 15$ nm. Atomic force microscopy (AFM) imaging of samples enabled to derive the topography of gold surfaces at the nanoscale reported in Figure 2f,g as a 2D density plot and in Figure 2h,i as a 3D plot. AFM datawere processed to derive the average Ra and root-mean-square Rrms values of surface roughness as Ra = 17 nm and Rrms = 22 nm. Further analysis with Fourier transform algorithms enabled us to derive the power spectrum density function $Q(q)$ associated with the clusters of gold nanoparticles (Figure 2j). A power spectrum reports the level of detail Q of a signal as a function of the spatial frequency q at which it is examined, as such it can be used to derive the fractal dimension D_f of a surface. If displayed in the form of a log−log plot, the power spectrum has the appearance of a line in the region of fractal behavior of the surface. From its slope, β, one can estimate the value of fractal dimension as $D_f = (8 - \beta)/2$, D_f being a measure of the complexity of a surface given as a change in details to a change of scale.[22] Using the methods previously described,[22] we determined for D_f the value $D_f \sim 2.4$ (to be noticed that the Euclidian dimension of a surface is D = 2). We point out that arrays of micropillars guarantee high

DOI: 10.1021/acsami.8b20501
ACS Appl. Mater. Interfaces 2019, 11, 3753−3762

values of contact angle (approaching 160°, see Figure 2k and Supporting Information (SI) Figure S1) provided that the solid fraction associated with those pillars is sufficiently small, a condition which makes the final contact angle of the device mostly ascribable to the microstructuration of the substrate and to a much less extent to its nanostructuration.

Simulating the EM Field around the Clusters of Gold Nanoparticles. We used finite element methods (FEM) to derive the distribution of the electromagnetic (EM) field around the gold nanoparticles of the device. We used AFM date to extract the topography and the roughness of the samples. Then, we generated a numerical parametric surface $f(x,y)$ given by the superposition of a finite series of sinusoidal waveforms as explained in the methods, with the same roughness and geometrical characteristics of the real physical prototype. In the model, f represent the gold nanotextured surface of the device, separating the silicon substrate from air in the remaining domain of the simulation (Figure 3a). We then simulated the distribution of the EM field in the system, for incident light of unit intensity $|E| = 1$ V/m and wavelength $\lambda = 633$ nm (Figure 3b). We found that on the rough gold surface the square intensity $|E|^2$ of the scattered radiation is ~1000 times higher than that of the initial disturbance (Figure 3b).

Recalling that metal enhanced fluorescence (MEF) effects are proportional to the square of the EM field,[20,21,29] diagram in Figure 3b indicates that site specific MEF enhancement factor associated with similar geometries is as high as $e_f = 10^3$. Since functionalization of the device is here operated through covalent attachment of an antigen−antibody complex to the gold surface (see next paragraph and Figure 4), with a hydrodynamic size comprised in the 10−30 nm interval, it has some interest examining the behavior of the EM field perpendicular away from the gold surface. Diagram in Figure 3c shows the variation of the EM square intensity $|E|^2$ along the normal to the gold surface z. Values of EM field are expressed as percentage of $|E|^2_0$, that is the value of $|E|^2$ measured on the gold surface $z = 0$. We observe that $|E|^2$ decreases slowly with z since at $z \sim 10$ nm from the surface, $|E|^2$ holds the 92% of its initial value, whereas at $z \sim 60$ nm from the surface, $|E|^2$ holds up to the 90% of its initial value. Amplification of the EM field and MEF effects are stable along z assuring optimal response of the device even if the measurement of target molecules is not carried out directly on the clusters of gold nanoparticles.

Fluorescence Lifetime Measurements and Imaging. The enhancement of the fluorescence was confirmed by the fluorescence lifetime imaging spectroscopy of labeled molecules specifically adsorbed on the nanostructured surface (SI Figure S2a). In fact, MEF induces an increase of the quantum yield of fluorescent molecules that can be ascribed to the reduction of the time spent in the excited state prior to return in the ground state.[30] This effect is evident form the difference between the lifetime of the fluorophore adsorbed onto the nanostructures lying in in the range 1.2−2.3 ns with a peak centered at 1.7 ns and the lifetime measured in the areas outside the nanostructures, which falls in the range 2.4−3.4 ns with a peak centered at 2.8 ns (SI Figure S2b). The latter value is similar to the lifetime of the native molecules measured directly in a drop (data not shown) thereby demonstrating the occurrence of the MEF process on the patterned gold nanostructures on our substrate.

Substrate Nanostructure Optimization. Aiming at optimizing the conditions for MEF, we measured the

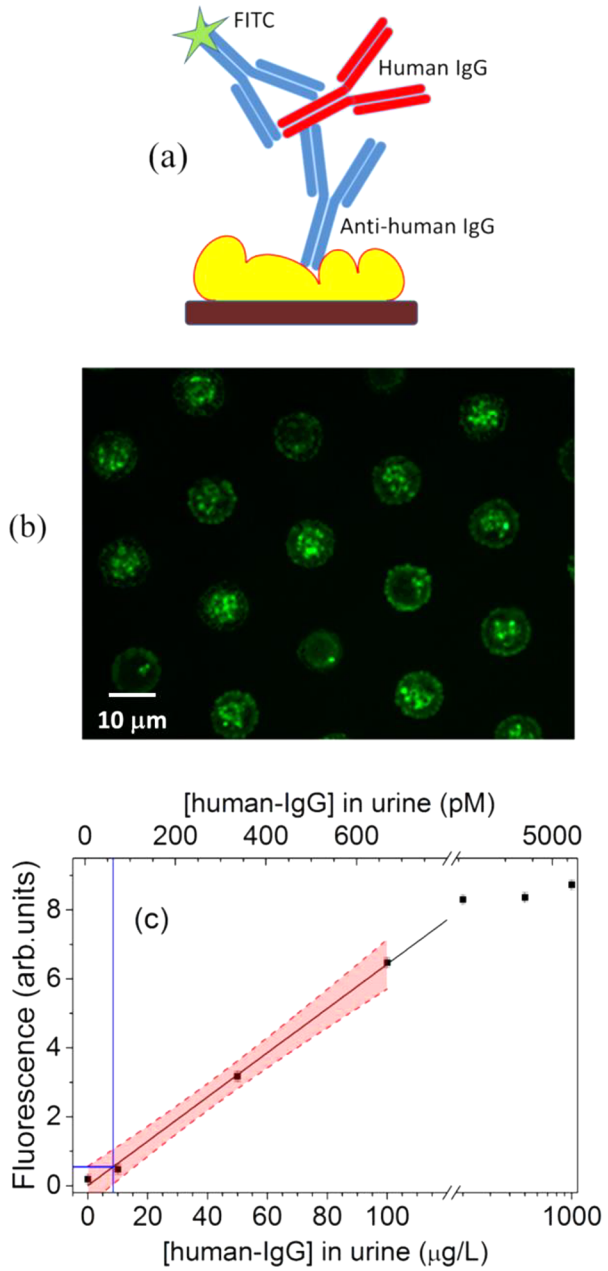

Figure 4. (a) Detection scheme: Antibodies tethered to the substrate by PIT recognize the antigen (human IgG). Secondary antibodies are tagged by FITC and bind the human IgG in a sandwich configuration. (b) Image of the substrate collected at [human IgG] = 200 μg/L with an integration time of 2 s and a magnification 50×. The lamp of the fluorescence microscope excites the FITC at 488 nm and the emitted light in the range 515−545 nm is collected. (c) Fluorescence intensity vs human IgG concentration. The area between the confidence bands at 95% level is highlighted in red.

fluorescence intensity on different gold surfaces (SI Figure S3a): "quasi flat", as it is the case for the gold electrode of a quartz-crystal microbalance and nanostructured with different quality grade of the gold nanoparticles (Au NPs), that is, low, medium, and high. The fluorescence from these four different substrates has been measure under the same functionalization conditions and the results are shown in Figure S3b. It is clearly visible that the "quasi flat" surface does not yield any fluorescence signal, whereas a strong signal is generated by the proper nanostructured surface (high quality grade). Since

DOI: 10.1021/acsami.8b20501
ACS Appl. Mater. Interfaces 2019, 11, 3753−3762

the quasi-flat surface belongs to a quartz-crystal microbalance (QCM) electrode, in this case we could check the correct surface functionalization and the subsequent presence of the fluorophores close to the surface by measuring the response provided by the QCM. The sensorgram is reported in SI Figure S4a and shows that the frequency shift produced by FITC-tagged IgG (≈160 Hz) is comparable to that produced by the functionalization (≈210 Hz), the latter corresponding to a fully covered surface.[31] The roughness of the "quasi-flat" electrode has been measured by AFM so that the response to electromagnetic field of the real surface could be analyzed by FEM (SI Figure S5), which confirms the lack of any amplification effect in this case. A similar analysis carried out on surfaces with different roughness (SI Figure S6) shows that the optimal geometry for MEF coincides with that used in this study (SI Figure S7). It is worth to mention that the occurrence of MEF leads to an increase of the fluorescence signal that can be detected even by cost-effective setup and with no particularly demanding environmental conditions.

Substrate Functionalization. The substrate described so far exhibits two main features: superhydrophobicity and metal nanostructured surface that entails the MEF. The actual case study we have chosen to test it as a biosensing platform concerns the assessment of the IgG content in urine for which no need for an extreme low limit of detection is required, but rather a robust and easy-to-use procedure is sought to attain a reliable point-of-care diagnostic tool. Thus, we decided to use a simple fluidic circuit that includes a cell where the substrate is placed for all the relevant steps of the measurement protocol such as functionalization, blocking, washing and interaction with the solution. Although superhydrophobicity is unavoidably lost, such an approach has proven to be more suitable for the aimed applications while keeping the main features of the device.

The gold surface of the substrate was functionalized by the photochemical immobilization technique (PIT), a quick, reproducible and effective procedure that is based on the selective photochemical reduction of the disulfide bridges in immunoglobulins produced by UV activation of the triad cysteine-cysteine/tryptophan,[32] the latter being a typical structural characteristic of the antibodies.[33] The UV photon is absorbed by the tryptophan and its photoreduction generates solvated electrons, which are captured by electrophilic species as cysteine resulting in the cleavage of the disulfide bridge. The free thiol groups so produced interact with gold surface leading to a covalent bond between the Ab and the gold surface. A recently reported characterization of UV-activated antibodies by means of atomic force microscopy showed that the PIT allows the immobilization of immunoglobulins onto gold surfaces in an upright orientation with their binding sites exposed to the environment.[26]

Calibration of the Biosensor. Human IgG was spiked into a urine sample from healthy subjects without proteinuria. The solution was conveyed to the functionalized substrate by the fluidic circuit described in SI Figure S8. The principle of detection of IgG and the resulting dose−response curve are reported in Figure 4. The antibodies (antihuman IgG) are tethered covalently to the nanostructured surface by means of PIT that binds them upright (Figure 4(a)). The human IgG in urine is recognized and captured by the primary Ab, so that a secondary fluorescent Ab (antihuman IgG tagged with FITC) is able to bind the Ab-antigen complex forming a sandwich structure. In view of the linear dimensions of the antibody, the distance between the fluorophore and the surface is expected to be 10−30 nm well within the effective distance leading to MEF, the latter being easily detected by examining the substrate under a standard fluorescence microscope (Leica DM 2700M). Typical image obtained by 50x objective is shown in Figure 4(b) where the disks are made visible by the fluorescence emission. For each concentration nine images like that reported in Figure 4(b) were analyzed so that the light from approximately 130 disks was integrated. The integration time of the microscope detector was only 2 s, a time chosen to be short enough to achieve a signal lying in the linear range of the setup response (see SI Figure S9). The fluorescence intensity measured at several human IgG concentrations is reported in Figure 4(c) with the best fit of the experimental data providing for the slope and intercept $m = 0.064 \pm 0.002$ L/μg and $n = 0.01 \pm 0.10$, respectively, with the goodness of the fit given by χ^2=3. The uncertainty about the single fluorescence measurement has been estimated to be ±0.15 at all the concentrations as a result of replicated experiments (duplicate and triplicate), which turns into an error of 2.3 μg/L. Thus, the relative error is less than 20% above [IgG] = 11.5 μg/L, which can be considered as the limit of quantification (LOQ).

Also shown in Figure 4c are the confidence bands at 95% confidence level, which include the area highlighted in red. The limit of detection can be estimated by considering that the upper limit (95% significance level) for the fluorescence signal at zero concentration corresponds to [human-IgG] ≈ 8 μg/L (blue segments in Figure 4c). Due to the kind of purification the urine underwent, IgGs at residual (physiological) level could still be in the matrix, but the standard deviation of the intercept (0.1 fluorescence units) and the calibration curve allow us to estimate an upper limit of approximately 3 μg/L at 95% (≈2 standard deviation). As a further additional test of our biosensor, we measured the signal produced by IgG at concentration of 5 μg/L in a filtered urine so to have a protein free matrix. In this case the response was 0.19 ± 0.15 fluorescence units (compatible with the calibration curve), that is, we achieved a "positive" answer which demonstrates the capability to detect such a low protein concentration.

As a final remark, we wish to point out that unlike other transduction mechanism like electrochemical or piezoelectric, the scheme depicted in Figure 4a does not depend on the size of the analyte, that is, the number of photons collected by the detector depend on the number of captured analyte rather than on their mass. Thus, in Figure 4c we also include as a scale on the top of the box the molarity conversion of the IgG concentration as so to provide the expectation of the proposed method with a generic analyte.

Validation of the Method. The validation of the method has been carried out by comparing the content of IgG in serum samples measured by a nephelometer with the output of the biosensor. Since the concentration of IgG in serum is well above the saturation limit of the biosensor, dilutions by 4−5 orders of magnitude were necessary to reach an IgG content in the linear range of SI Figure S9. The results of this measurements are reported in Figure 5 (black square points) and are well fitted by a linear curve with a slope $m = 1.01 \pm 0.03$ and an intercept $n = -0.35 \pm 0.37$ g/L.

The knowledge of the hematocrit (H) for each of the whole sample allowed us to assess the expected IgG concentration in blood by the formula $[\mathrm{IgG}]_{\mathrm{blood}} = [\mathrm{IgG}]_{\mathrm{serum}}(1 - H)$. Such a concentration can be actually measured by the MEF based

DOI: 10.1021/acsami.8b20501
ACS Appl. Mater. Interfaces 2019, 11, 3753−3762

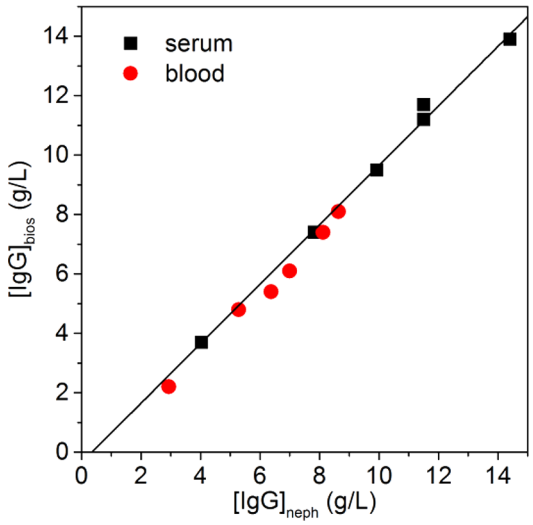

Figure 5. Linear regression analysis of IgG levels in serum (black square points, $n = 6$) determined by biosensor and nephelometer. The biosensor has been used to measure [IgG] even in whole blood (red circle points).

biosensor since—unlike the nephelometer—its high sensitivity allows a significant dilution of the sample that can be safely sent through the fluidic circuit. The results of the measurement of [IgG] in blood are reported as red circle points in Figure 5 and the agreement with the calibration straight line is impressive. Thus, while the results in sera demonstrate the reliability of the proposed biosensor that is able to compare with the reference technology provided by the nephelometer even after high dilution, the agreement of IgG values in blood with calculated values paves the way to applications of the biosensor to the direct analysis of tiny amount of untreated whole blood.

IgG Assessment in Urine Sample. The importance of POC devices for detecting proteins, and specifically IgGs, in urine is 3-fold. First, several authors hypothesize the presence of small and, to a lesser extent, large pores, in the glomerular filtration barrier of healthy subjects, which allow the leakage of albumin (68 kDa), and small amounts of proteins with higher molecular weight such as IgG (≈150 kDa), respectively, whereas no larger pore is expected to allow leakage of very large immunoglobulins such as IgM (≈1000 kDa).[34−36] In case of kidney injury, the glomerular filtration barrier does not work properly thereby causing significant presence of proteins in urines (proteinuria), and according to the size of proteins, proteinuria is defined (i) selective, when the most excreted proteins are albumin and transferrin, or (ii) nonselective, when high molecular weight proteins are also excreted in addition to albumin and transferrin.[37] Second, proteinuria is a frequent kidney post-transplant event probably due to ischemic reperfusion injury of the native kidney or allograft, although it tends to drop within a few weeks in case of successful transplantation or to persists (or even to appear later) in the opposite case.[37] Third, in view of early detection of transplantation damage and rapid clinical intervention, the surveillance biopsies is considered of high importance in the post-transplant monitoring in children since they are at higher risk for allograft damage due to both the different size of the transplanted kidney and the greater immunological response.[38] The clinical outcomes of the several molecular injury, immunological, and nonimmunological, can be acute cellular rejection, interstitial fibrosis and tubular atrophy, microvascular lesions, and transplant glomerulopathy. In particular, patients with interstitial fibrosis and tubular atrophy plus inflammation had higher levels of urinary IgG.[39]

In view of the above considerations the evaluation of even minimal urinary changes in IgG levels is of great importance for the monitoring of patients with renal impairment or for the monitoring of patients transplanted with renal allograft, particularly the children. This is not achievable by the standard reference method based on the nephelometer,[40] since it does not provide the required sensitivity. On the other hand, novel methods like Luminex-based immunoassays,[36] although suitable in terms of sensitivity, lack the easiness of use and the swiftness required to a POC device.

The appropriateness of the device proposed here has been tested on real samples of urine to check possible cross-reactions entailed by the presence of other proteins and/or molecules. The results are reported in SI Table S1 where the first line shows [IgG] measure in a pool of samples from five people for whom no protein exceeded the normal value. The following lines reports the values of IgG measured by the MEF-based biosensor in urine from people with altered values of hemoglobin, bilirubin, free light chain (κ and λ) and urobilinogen, which represent a wide range of proteins that may be present in urine. Even after dilution, we observed no significant change of IgG concentration (interference leads to nonlinear response in serial dilutions), only hemoglobin giving rise to a small underestimation of IgG content.

In addition, IgG levels were measured in a sample with low total proteinuria of 600 mg/L (SI Table S2). In this pathological sample we obtained a value higher than the saturation limit of the biosensor (200 μg/L), so we performed the analysis of IgG on two dilutions (1.500 and 1:1000) that provided 50 ± 5 mg/L and 60 ± 5 mg/L, respectively. It is worth noticing that such values show the occurrence of no interference effects in a real pathological case and are approximately 10% of the total excretion of the proteins, a value in very good agreement with the literature.[36] Moreover, it is noticeable to observe that the value obtained in our urine sample, that is, 50−60 mg/L is barely above the limit of detection of nephelometric method.

CONCLUSIONS

We developed an immunosensor where the enhancement of the fluorescence signal generated by patterned gold nanoparticles combines with the high selectivity of a biological functionalization to yield a highly sensitive, specific and reliable device. Additional characteristics including limited size, portability, and cost-effectiveness, make this medical device ideal for being utilized at the point of care of a patient. The device detects IgGs directly from a drop of urine of a patient. The analysis necessitates of a conventional fluorescence microscope and may last, in a more sophisticated evolution of the technique, few minutes. Tests indicated that the device has a limit of detection smaller than 10 μg/L with a linear response in the range 10−100 μg/L. Additional tests in complex biological mixtures and in blood showed that the performance of the device is not affected to any extent by interfering substances including proteins. The performance of the device was validated using nephelometry, that is the current gold standard for analysis in immunology. Results from the analysis with the device (conducted in urine with diluted analytes) and from the standard (conducted in serum with

DOI: 10.1021/acsami.8b20501
ACS Appl. Mater. Interfaces 2019, 11, 3753−3762

concentrated analytes) showed excellent agreement between the device and standard techniques, and suggest that our device can potentially detect proteins in the low abundance ranges of 100 pM from whole blood.

Currently, the whole experimental setup includes a UV lamp for Ab activation, a simple fluidic circuit and a fluorescence microscope. The commercial availability of fluorescence microplate readers as well as of fluidic circuits makes it possible to design a platform that incorporates both items together with the UV lamp necessary for Ab activation (PIT). Since each of the parts can be already run in a controlled way, we can envisage the possibility to operate the whole system, which turns out to be portable, and the measurement procedure to a high degree of automation.

In the present configuration, the microfluidic setup integrated with the nanoscale substrate impairs superhydrophobicity of the device. On the other hand, the microfluidic system enables to deliver controlled volumes of solution on the device assuring repeatability, reproducibility, and reducing uncertainty. Alternative approaches to microfluidics may enable to preserve the superhydrophobicity of the substrate and exploit its benefits. For instance, noncontact microdispensing systems offer accurate and high-throughput deposition of fluids on a substrate and since it is a noncontact technology, droplet microdispensing can be used to deposit biological fluids on the device with high precision without disabling its superhydrophobic characteristics. A recovered superhydrophobic effect can improve the performance of the device in several aspects (see SI Figure S10) since it enables (i) concentration of a solute into small areas and relative enhancement of the fluorescence signal, (ii) precise positioning of the drop on the active sites of the device, (iii) multiplexing.

MATERIALS AND METHODS

Fabrication of the Device. We cleaned P type (100) Silicon wafers with acetone, then substrates were spin-coated with a S1813 positive tone resist (from Rohm and Haas). Optical lithography (Karl Suss Mask Aligner MA 45, Suss MicroTec GA, Garching, Germany) was used to generate hexagonal patterns of holes in the resist, with nominal diameter $d = 10\ \mu$m and gap $\delta = 20\ \mu$m. The diameter to gap ratio 1:2 guaranties the best compromise between elevated antifouling characteristic and good stability of the device.[28] Gold nanoparticles were deposited within the holes using electroless deposition following the methods previously described.[22] The residual resist was removed with acetone, samples were then processed using deep reactive ion etching (DRIE) techniques (MESC Multiplex ICP, STS, Imperial Park, Newport, UK) to extrude the initial pattern and generate 2 + 1-dimensional arrays of cylindrical pillars with height $h = 15\ \mu$m. Subsequently, samples were covered with a thin film of C_4F_8 polymer. The optical lithography masks were fabricated using direct writing with Electron Beam Lithography (Crestec CABL-9000C electron beam lithography system). The DRIE process is a pulsed etching that alternated cyclically between three modes: (i) deposition of the passivation layer C_4F_8; (ii) isotropic plasma etch with SF_6; and (iii) sample/chamber cleaning. The proportion between the passivation and etching times was adjusted to ensure verticality of pillar walls.

Photochemical Immobilization Technique. In this experiment the implementation of PIT was carried out by irradiating a solution of 50 μg/mL antihuman IgG for 1 min by a HERAEUS amalgam type NNI 40/20 lamp emitting at 254 nm with a power of 40 W. The lamp was approximately 20 cm long and had a diameter of 1 cm, so that the intensity was about 0.7 W/cm^2 very close to the surface. By considering that the cuvette containing the antihuman IgG solution was located at 1 cm from the lamp surface, the effective irradiation intensity used for the antibody activation was about 0.3 W/cm^2. The irradiation time used for PIT is the result of an optimized protocol that warrants no denaturation of antibodies, as demonstrated by their effectiveness in biosensing, while yielding high concentration of UV-activated Abs, as measured by the Ellman assay.[41] The activated Abs were then conveyed to the substrate by means of a fluidic circuit (SI Figure S8). It is worth mentioning that PIT does not affect the intrinsic selectivity of the antibodies; indeed, this method has been used in a number of experiments with quartz crystal microbalances[42−44] as well as with colorimetric biosensors.[45]

SEM Sample Characterization. SEM images of the pillars and the gold nanoparticles clusters were captured using a Dual Beam (SEM-FIB) - FEI Nova 600 NanoLab system. The beam energy and the corresponding electron current were set as 15 keV and 0.14 nA throughout the acquisitions.

AFM Sample Characterization. Atomic force microscopy (ICON) was used for sample characterization. All the measurements were performed in a dry environment in intermittent contact mode over sampling areas of 1 μm × 1 μm and 500 nm × 500 nm. Room temperature was hold fixed for all the acquisitions. Ultrasharp Si probes with a nominal tip radius less than 5 nm were used for achieving high resolution. Multiple measurements were done in different scan directions to avoid artifacts. At least four images in height mode (trace and retrace) were recorded per each sample. The images had a resolution of 512 × 512 points and were acquired at a scanning rate of 1 Hz. Fast Fourier transform algorithms enabled post processing of images and decoding of the information content of the images.

Deriving the Fractal Dimension of the Samples. The AFM profiles of the clusters of gold nanoparticles were processed by homemade algorithms. In doing so, we derived for each image a characteristic power spectrum density function. A power spectrum is function that delivers the information content of an image as a function of scale. In a log−log plot, it appears as a line with slope β. The fractal dimension D_f of a surface can be derived from β as $D_f = (8 - \beta)/2$. The fractal dimension of a surface can take noninteger values, and ranges between 2 for a nominally flat Euclidean surface to 3 for a surface that ideally fills all the space within which it is embedded.

Measuring Sample Wettability. Surface hydro-phobicity of the samples was determined by measuring the water contact angle with one drop of deionized water using an automatic contact angle meter (KSV CAM 101, KSV Instruments LTD, Helsinki, Finland) at room temperature. Four measurements were performed on each substrate to evaluate the average contact angle θ, at 5 s.

Simulating the EM Field around the Gold Nanoparticles. We used finite element methods (FEM) and the commercial software COMSOL Multiphysics 5.3 to simulate the EM field around the gold nanoparticles. We examined the behavior of the particles using 3D (reported in the main text) and 2D (SI Figures S11−S12) schemes built using the topography of the real physical prototype extracted from AFM data. The volume of the simulations was divided into three domains, that is, (i) air, (ii) a supporting silicon substrate with constant refractive index $n_{Si} = 3.48$, and (iii) a layer of gold Au rough nanoparticles, represented using the complex dielectric constant of a gold dielectric provided by Rakic and co-workers.[46] For the thee-dimensional configuration, we have represented the layer of gold nanoparticles as a parametric surface $z = f(x, y)$, with x, y, and z the spatial coordinates of the system, and f a function of x and y. We used for f a truncated Fourier series of sine waves of certain discrete spatial frequencies: $f(x,y) = \sum_{m,n} f_{m,n}(x,y)$. Space oscillations of the surface are governed by the spatial frequencies of each of the sine waves $f_{m,n}$:

$$f_{m,n}(x, y) = A_{m,n}\cos(\bar{k}_{m,n}\cdot\bar{x} + \phi) = A_{m,n}\cos(2\pi(mx + ny) + \phi) \quad (1)$$

where $A_{m,n}$ is the amplitude, ϕ is a random phase factor, m and n are the spatial frequencies along x and y; $\bar{k}_{m,n}$ is the wavenumber defining the propagation of each sine wave with respect to the unit vector $\bar{x}$. We then defined a cutoff frequency N representing to the maximum value of frequency that m and n can assume, thus the smallest feature representable in the system is $\lambda_{min} = 1/N$. The random phase term is

DOI: 10.1021/acsami.8b20501
ACS Appl. Mater. Interfaces 2019, 11, 3753−3762

sampled from an uniform random distribution comprised in the $0 - \pi$ interval. Instead, the amplitude is expressed as

$$A_{m,n} = \frac{G(m, n)}{(m^2 + n^2)^{\beta/2}} \quad (2)$$

with $G(m,n)$ a Gaussian distribution and β a spectral exponent. On tuning β, one can choose how fast higher frequencies are attenuated, that in turn enables to describe random smooth amplitude variations. Combining eqs 1 and 2, one obtains a complete description of the gold surface topography:

$$(x, y) = \sum_{m=-N}^{N} \sum_{n=-N}^{N} \frac{G(m, n)}{(m^2 + n^2)^{\beta/2}} \cos(2\pi(mx + ny) + \phi(m, n)) \quad (3)$$

where convenient preconditioning of eq 3 with a prefactor avoids spikes due to high frequency oscillations. Maxwell equations were then resolved and the EM field was derived everywhere within the domain of interest. The stimulus, that is, the incident electric field $\bar{E}_0$, is perpendicular to the gold surface, is linearly polarized along $\bar{x}$, has modulus $|\bar{E}_0| = 1\ V/m$ and wavelength $\lambda = 633$ nm. The simulation domain was truncated using perfectly matched layers (PML) at the upper and lower boundaries of the system. Symmetry of the system was exploited to use a quarter of the model and reduce simulation times. Perfect electric and magnetic conductor conditions have been imposed.

Biological Samples and Biochemical Analyses. Normal urine samples ($n = 5$) and urine samples each containing one potential interfering compound, that is, hemoglobin (0.15 mg/dL), bilirubin (12 mg/dL), free light chains kappa (363 mg/L) and lambda (790 mg/L), urobilinogen (7 mg/dL), were anonymously selected from samples already analyzed in our laboratories (SI Table S1). In addition, an urine sample with low proteinuria (SI Table S2) was also selected and total protein concentration was accurately determined by Bradford method.[47]

Protein free urine sample was obtained by centrifugal ultrafiltration of normal urine sample used for calibration of the biosensor. In particular, the urine sample was filtered by Centricon 3 (Amicon, W.R. Grace & Co. − Conn., Beverly, MA) with a molecular weight cut off of 3 kDa. The ultrafiltration was performed by centrifugation of 2 mL of sample at 4000 rpm for 2 h.

Furthermore, serum samples ($n = 6$) and the corresponding blood samples in EDTA tubes, with known hematocrit value ($n = 6$), were randomly selected from samples already analyzed in our laboratories. For method validation, total IgG were determined in serum samples by BN II System nephelometer (Siemens Healthcare Diagnostics s.r.l., Milano, Italy). The comparison between methods was performed by linear regression analysis.

■ ASSOCIATED CONTENT

Supporting Information

The Supporting Information is available free of charge on the ACS Publications website at DOI: 10.1021/acsami.8b20501.

Expected contact angle of a superhydrophobic surface (S1). Fluorescence lifetime measurements and imaging (S2). Substrate nanostructure optimization (S3). QCM check of the correct surface functionalization of the flat gold electrode with human IgG (S4). FEM simulations of MEF on the gold flat surface (S5). MEF optimization of the geometry of the gold-nanoparticles (S6−S7). Fluidic circuit (S8). Calibration of the detector (S9). Practical advantages of a superhydrophobic surface in the analysis of analytes (S10). 2D numerical model and simulations (S11−S12). IgG concentrations determined by biosensor in urine samples with and without potential interfering compounds (Table S1). IgG concentration determined by biosensor in a urine sample with low proteinuria (Table S2) (PDF)

■ AUTHOR INFORMATION

Corresponding Authors

*(E.B.) E-mail: edmondo.battista@unina.it.
*(F.G.) E-mail: francesco.gentile2@unina.it.
*(R.V.) E-mail: rvelotta@unina.it.

ORCID

Edmondo Battista: 0000-0003-0915-9176
Alessandro Alabastri: 0000-0001-6180-8052
Francesco Gentile: 0000-0002-1724-6301
Raffaele Velotta: 0000-0003-1077-8353

Author Contributions

The manuscript was written through contributions of all authors. B.D.V. and M.G. contributed equally to this work.

Notes

The authors declare no competing financial interest.

■ ABBREVIATIONS

POC	point of care
Ab	antibody
LOD	limit of detection
PIT	photochemical immobilization technique
OECT	organic electrochemical transistor
EM	electromagnetic

■ REFERENCES

(1) Florkowski, C.; Don-Wauchope, A.; Gimenez, N.; Rodriguez-Capote, K.; Wils, J.; Zemlin, A. Point-of-Care Testing (POCT) and Evidence-Based Laboratory Medicine (EBLM)−does It Leverage Any Advantage in Clinical Decision Making? *Crit. Rev. Clin. Lab. Sci.* **2017**, *54* (7−8), 471−494.

(2) Baryeh, K.; Takalkar, S.; Lund, M.; Liu, G. Introduction to Medical Biosensors for Point of Care Applications. In *Medical Biosensors for Point of Care (POC) Applications*; Narayan, R. J., Ed.; Elsevier Ltd, 2016; pp 3−25.

(3) Syedmoradi, L.; Daneshpour, M.; Alvandipour, M.; Gomez, F. A.; Hajghassem, H.; Omidfar, K. Point of Care Testing: The Impact of Nanotechnology. *Biosens. Bioelectron.* **2017**, *87* (2017), 373−387.

(4) Hodson, R. Precision Medicine. *Nature* **2016**, *537* (7619), S49−S49.

(5) Ferrari, M. Cancer Nanotechnology: Opportunities and Challenges. *Nat. Rev. Cancer* **2005**, *5* (3), 161−171.

(6) Shi, J.; Kantoff, P. W.; Wooster, R.; Farokhzad, O. C. Cancer Nanomedicine: Progress, Challenges and Opportunities. *Nat. Rev. Cancer* **2017**, *17* (1), 20−37.

(7) Lim, E.-K.; Kim, T.; Paik, S.; Haam, S.; Huh, Y.-M.; Lee, K. Nanomaterials for Theranostics: Recent Advances and Future Challenges. *Chem. Rev.* **2015**, *115* (1), 327−394.

(8) Li, Y.; Wang, Y.; Huang, G.; Gao, J. Cooperativity principles in self-assembled nanomedicine. *Chem. Rev.* **2018**, DOI: 10.1021/acs.chemrev.8b00195.

(9) Jiang, W.; von Roemeling, C. A.; Chen, Y.; Qie, Y.; Liu, X.; Chen, J.; Kim, B. Y. S. Designing Nanomedicine for Immuno-Oncology. *Nat. Biomed. Eng.* **2017**, *1* (2), 0029.

(10) Anchordoquy, T. J.; Barenholz, Y.; Boraschi, D.; Chorny, M.; Decuzzi, P.; Dobrovolskaia, M. A.; Farhangrazi, Z. S.; Farrell, D.; Gabizon, A.; Ghandehari, H.; Godin, B.; La-Beck, N. M.; Ljubimova, J.; Moghimi, S. M.; Pagliaro, L.; Park, J.-H.; Peer, D.; Ruoslahti, E.; Serkova, N. J.; Simberg, D. Mechanisms and Barriers in Cancer Nanomedicine: Addressing Challenges, Looking for Solutions. *ACS Nano* **2017**, *11* (1), 12−18.

(11) Gentile, F.; Ferrara, L.; Villani, M.; Bettelli, M.; Iannotta, S.; Zappettini, A.; Cesarelli, M.; Di Fabrizio, E.; Coppedè, N.

DOI: 10.1021/acsami.8b20501
ACS Appl. Mater. Interfaces 2019, 11, 3753−3762

Geometrical Patterning of Super-Hydrophobic Biosensing Transistors Enables Space and Time Resolved Analysis of Biological Mixtures. *Sci. Rep.* **2016**, *6* (1), 18992.
(12) da Silva, E. T. S. G.; Souto, D. E. P.; Barragan, J. T. C.; de F. Giarola, J.; de Moraes, A. C. M.; Kubota, L. T. Electrochemical Biosensors in Point-of-Care Devices: Recent Advances and Future Trends. *ChemElectroChem* **2017**, *4* (4), 778−794.
(13) Coppedè, N.; Villani, M.; Gentile, F. Diffusion Driven Selectivity in Organic Electrochemical Transistors. *Sci. Rep.* **2015**, *4* (1), 4297.
(14) Bauch, M.; Toma, K.; Toma, M.; Zhang, Q.; Dostalek, J. Plasmon-Enhanced Fluorescence Biosensors: A Review. *Plasmonics* **2014**, *9* (4), 781−799.
(15) Strobbia, P.; Languirand, E.; Cullum, B. M. Recent Advances in Plasmonic Nanostructures for Sensing: A Review. *Opt. Eng.* **2015**, *54* (10), 100902.
(16) Yesilkoy, F.; Terborg, R. A.; Pello, J.; Belushkin, A. A.; Jahani, Y.; Pruneri, V.; Altug, H. Phase-Sensitive Plasmonic Biosensor Using a Portable and Large Field-of-View Interferometric Microarray Imager. *Light: Sci. Appl.* **2017**, *7* (2), 17152.
(17) Belushkin, A.; Yesilkoy, F.; Altug, H. Nanoparticle-Enhanced Plasmonic Biosensor for Digital Biomarker Detection in a Microarray. *ACS Nano* **2018**, *12*, 4453.
(18) Lin, R.; Li, C.; Chen, Y.; Liu, F.; Li, N. Metal-Enhanced Fluorescence in Biosensing Applications. In *Surface Plasmon Enhanced, Coupled and Controlled Fluorescence*; Geddes, C. D., Ed.; John Wiley & Sons, Inc.: Hoboken, NJ, 2017; pp 121−136.
(19) De Angelis, F.; Gentile, F.; Mecarini, F.; Das, G.; Moretti, M.; Candeloro, P.; Coluccio, M. L.; Cojoc, G.; Accardo, A.; Liberale, C.; Zaccaria, R. P.; Perozziello, G.; Tirinato, L.; Toma, A.; Cuda, G.; Cingolani, R.; Di Fabrizio, E. Breaking the Diffusion Limit with Super-Hydrophobic Delivery of Molecules to Plasmonic Nanofocusing SERS Structures. *Nat. Photonics* **2011**, *5* (11), 682−687.
(20) Deng, W.; Xie, F.; Baltar, H. T. M. C. M.; Goldys, E. M. Metal-Enhanced Fluorescence in the Life Sciences: Here, Now and Beyond. *Phys. Chem. Chem. Phys.* **2013**, *15* (38), 15695.
(21) Ray, K.; Lakowicz, J. R. Metal-Enhanced Fluorescence Lifetime Imaging and Spectroscopy on a Modified SERS Substrate. *J. Phys. Chem. C* **2013**, *117* (30), 15790−15797.
(22) Battista, E.; Coluccio, M. L.; Alabastri, A.; Barberio, M.; Causa, F.; Netti, P. A.; Di Fabrizio, E.; Gentile, F. Metal Enhanced Fluorescence on Super-Hydrophobic Clusters of Gold Nanoparticles. *Microelectron. Eng.* **2017**, *175*, 7−11.
(23) Wang, H.; Yuan, X.; Zeng, G.; Wu, Y.; Liu, Y.; Jiang, Q.; Gu, S. Three Dimensional Graphene Based Materials: Synthesis and Applications from Energy Storage and Conversion to Electrochemical Sensor and Environmental Remediation. *Adv. Colloid Interface Sci.* **2015**, *221*, 41−59.
(24) Wang, X.; Li, S.; Zhang, P.; Lv, F.; Liu, L.; Li, L.; Wang, S. An Optical Nanoruler Based on a Conjugated Polymer−Silver Nanoprism Pair for Label-Free Protein Detection. *Adv. Mater.* **2015**, *27* (39), 6040−6045.
(25) Cui, Q.; He, F.; Li, L.; Möhwald, H. Controllable Metal-Enhanced Fluorescence in Organized Films and Colloidal System. *Adv. Colloid Interface Sci.* **2014**, *207*, 164−177.
(26) Funari, R.; Della Ventura, B.; Altucci, C.; Offenhäusser, A.; Mayer, D.; Velotta, R. Single Molecule Characterization of UV-Activated Antibodies on Gold by Atomic Force Microscopy. *Langmuir* **2016**, *32* (32), 8084−8091.
(27) Lafuma, A.; Quéré, D. Superhydrophobic States. *Nat. Mater.* **2003**, *2* (7), 457−460.
(28) Papadopoulos, P.; Mammen, L.; Deng, X.; Vollmer, D.; Butt, H.-J. How Superhydrophobicity Breaks Down. *Proc. Natl. Acad. Sci. U. S. A.* **2013**, *110* (9), 3254−3258.
(29) Tabakman, S. M.; Lau, L.; Robinson, J. T.; Price, J.; Sherlock, S. P.; Wang, H.; Zhang, B.; Chen, Z.; Tangsombatvisit, S.; Jarrell, J. A.; Utz, P. J.; Dai, H. Plasmonic Substrates for Multiplexed Protein Microarrays with Femtomolar Sensitivity and Broad Dynamic Range. *Nat. Commun.* **2011**, *2* (1), 466.
(30) Das, G.; Battista, E.; Manzo, G.; Causa, F.; Netti, P. A.; Di Fabrizio, E. Large-Scale Plasmonic NanoCones Array For Spectroscopy Detection. *ACS Appl. Mater. Interfaces* **2015**, *7* (42), 23597−23604.
(31) Della Ventura, B.; Schiavo, L.; Altucci, C.; Esposito, R.; Velotta, R. Light Assisted Antibody Immobilization for Bio-Sensing. *Biomed. Opt. Express* **2011**, *2* (11), 3223−3231.
(32) Neves-Petersen, M. T.; Gryczynski, Z.; Lakowicz, J.; Fojan, P.; Pedersen, S.; Petersen, E.; Bjørn Petersen, S. High Probability of Disrupting a Disulphide Bridge Mediated by an Endogenous Excited Tryptophan Residue. *Protein Sci.* **2002**, *11* (3), 588−600.
(33) Ioerger, T. R.; Du, C.; Linthicum, D. S. Conservation of Cys−cys Trp Structural Triads and Their Geometry in the Protein Domains of Immunoglobulin Superfamily Members. *Mol. Immunol.* **1999**, *36* (6), 373−386.
(34) Ohlson, M.; Sörensson, J.; Lindström, K.; Blom, A. M.; Fries, E.; Haraldsson, B. Effects of Filtration Rate on the Glomerular Barrier and Clearance of Four Differently Shaped Molecules. *Am. J. Physiol. Physiol.* **2001**, *281* (1), F103−F113.
(35) D'Amico, G.; Bazzi, C. Pathophysiology of Proteinuria. *Kidney Int.* **2003**, *63* (3), 809−825.
(36) Gohda, T.; Walker, W. H.; Wolkow, P.; Lee, J. E.; Warram, J. H.; Krolewski, A. S.; Niewczas, M. A. Elevated Urinary Excretion of Immunoglobulins in Nonproteinuric Patients with Type 1 Diabetes. *Am. J. Physiol. Physiol.* **2012**, *303* (1), F157−F162.
(37) Ponticelli, C.; Graziani, G. Proteinuria after Kidney Transplantation. *Transplant Int.* **2012**, *25* (9), 909−917.
(38) Birk, P. E. Surveillance Biopsies in Children Post-Kidney Transplant. *Pediatr. Nephrol.* **2012**, *27* (5), 753−760.
(39) Amer, H.; Lieske, J. C.; Rule, A. D.; Kremers, W. K.; Larson, T. S.; Palacios, C. R. F.; Stegall, M. D.; Cosio, F. G. Urine High and Low Molecular Weight Proteins One-Year Post-Kidney Transplant: Relationship to Histology and Graft Survival. *Am. J. Transplant.* **2013**, *13* (3), 676−684.
(40) Warren, J. S. Immunoglobulin Quantification and Viscosity Measurement. In *Manual of Molecular and Clinical Laboratory Immunology*,7th ed.; Detrick, B., Hamilton, R., Folds, J., Eds.; American Society of Microbiology: Washington, DC,, 2006; pp 69−74.
(41) Ellman, G. L. Tissue Sulfhydryl Groups. *Arch. Biochem. Biophys.* **1959**, *82* (1), 70−77.
(42) Funari, R.; Della Ventura, B.; Carrieri, R.; Morra, L.; Lahoz, E.; Gesuele, F.; Altucci, C.; Velotta, R. Detection of Parathion and Patulin by Quartz-Crystal Microbalance Functionalized by the Photonics Immobilization Technique. *Biosens. Bioelectron.* **2015**, *67*, 224−229.
(43) Della Ventura, B.; Sakač, N.; Funari, R.; Velotta, R. Flexible Immunosensor for the Detection of Salivary α-Amylase in Body Fluids. *Talanta* **2017**, *174*, 52−58.
(44) Della Ventura, B.; Iannaccone, M.; Funari, R.; Pica Ciamarra, M.; Altucci, C.; Capparelli, R.; Roperto, S.; Velotta, R. Effective Antibodies Immobilization and Functionalized Nanoparticles in a Quartz-Crystal Microbalance-Based Immunosensor for the Detection of Parathion. *PLoS One* **2017**, *12* (2), e0171754.
(45) Iarossi, M.; Schiattarella, C.; Rea, I.; De Stefano, L.; Fittipaldi, R.; Vecchione, A.; Velotta, R.; Della Ventura, B. Colorimetric Immunosensor by Aggregation of Photochemically Functionalized Gold Nanoparticles. *ACS Omega* **2018**, *3* (4), 3805−3812.
(46) Rakić, A. D.; Djurišić, A. B.; Elazar, J. M.; Majewski, M. L. Optical Properties of Metallic Films for Vertical-Cavity Optoelectronic Devices. *Appl. Opt.* **1998**, *37* (22), 5271−5283.
(47) Bradford, M. M. A Rapid and Sensitive Method for the Quantitation of Microgram Quantities of Protein Utilizing the Principle of Protein-Dye Binding. *Anal. Biochem.* **1976**, *72* (1−2), 248−254.

DOI: 10.1021/acsami.8b20501
ACS Appl. Mater. Interfaces 2019, 11, 3753−3762